ARTICLE

Theoretical Insights into Oxygen Reduction Reaction on Au-Based Single-Atom Alloy Cluster Catalysts†

Yixuan Pu[a], Jin-Xun Liu[a,b*]

a. Key Laboratory of Precision and Intelligent Chemistry, School of Chemistry and Materials Science, University of Science and Technology of China, Hefei 230026, China
b. Hefei National Laboratory, University of Science and Technology of China, Hefei 230088, China

(Dated: Received on May 25, 2024; Accepted on August 12, 2024)

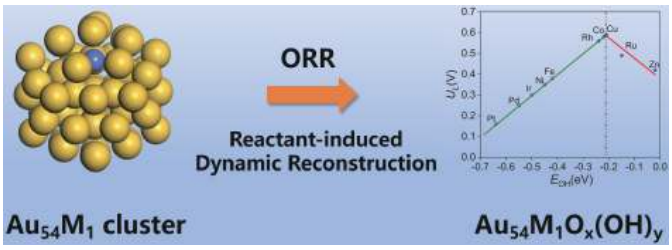

Developing highly active alloy catalysts that surpass the performance of platinum group metals in the oxygen reduction reaction (ORR) is critical in electrocatalysis. Gold-based single-atom alloy (AuSAA) clusters are gaining recognition as promising alternatives due to their potential for high activity. However, enhancing its activity of AuSAA clusters remains challenging due to limited insights into its actual active site in alkaline environments. Herein, we studied a variety of $Au_{54}M_1$ SAA cluster catalysts and revealed the operando formed $MO_x(OH)_y$ complex acts as the crucial active site for catalyzing the ORR under the basic solution condition. The observed volcano plot indicates that $Au_{54}Co_1$, $Au_{54}Cu_1$, and $Au_{54}Ru_1$ clusters can be the optimal $Au_{54}M_1$ SAA cluster catalysts for the ORR. Our findings offer new insights into the actual active sites of AuSAA cluster catalysts, which will inform rational catalyst design in experimental settings.

Key words: Density functional theory, Single-atom alloy cluster, Oxygen reduction reaction, Gold cluster, Molecular dynamic simulation

I. INTRODUCTION

The oxygen reduction reaction (ORR) represents a pivotal electrochemical process, particularly critical in the cathodes of fuel cells and metal-air batteries. Effective catalysis of the ORR is essential for boosting the efficiency and reducing the operational costs of these green energy solutions [1–10]. This reaction primarily reduces oxygen molecules into water or hydroxide ions, depending on the environmental conditions [11]. Historically, platinum and its alloys have set the standard for ORR catalysts due to their unmatched catalytic performance and robust stability [12–17]. However, the substantial cost and limited availability of platinum have spurred a significant shift towards exploring alternative materials [18–23]. This drive aims to discover new catalysts that maintain or surpass the efficacy of platinum while mitigating its economic and logistical drawbacks.

Strategies to improve the ORR performance of catalysts involve engineering nanostructures in multimetallic alloys to enhance their activity and stability by adjusting electronic and geometric structures and leveraging synergistic effects of catalysts [21, 24–32]. Diminishing the size of catalyst particles to the scale of clusters presents another promising approach. Cluster catalysts featuring dispersed atomic configurations hold great promise for advancing catalytic processes across various industries including ORR [33–37]. The clusters, of-

† Part of Special Topic "Theoretical and Computational Catalysis".

* Author to whom correspondence should be addressed. E-mail: jxliu86@ustc.edu.cn

 © 2024 Chinese Physical Society

ten comprising a small number of atoms, exhibit unique reactivity and selectivity due to their high surface-to-volume ratio and well-defined structures [34]. Gold metal has been explored as a potential alternative to expensive catalysts for the ORR in alkaline environments compared to Pt-based catalysts. Several gold and gold nanoalloys, including AuAg [38], AuPtCo [39], and AuPtPd [40] nanoalloys, have been investigated for their efficient electrocatalytic performance in facilitating the ORR in alkaline fuel cells and batteries. Especially, gold-silver alloy nanoclusters composed of Au_1Ag_{21} single-atom alloys supported on activated carbon have exhibited exceptional ORR activity in alkaline solutions [41]. However, ORR mechanisms and active sites in Au-based SAA catalysts remain poorly understood, posing significant challenges to their rational design. Clarifying these mechanisms and active sites is essential to predict and engineer Au-based catalysts that outperform traditional Pt catalysts in activity, thereby advancing ORR catalyst technology.

In the present work, extensive multiple theoretical modeling approach was conducted to reveal the active site of Au single atom alloy (AuSAA) [42–47] clusters in the ORR under aqueous alkaline conditions. Using the $Au_{54}Co_1$ SAA cluster catalyst as a case study, we integrated *ab initio* molecular dynamics (AIMD) simulations with *ab initio* thermodynamic analysis to examine the dynamic behavior of Co atoms. We observed that Co_1 atom could migrate from the subsurface to the surface of the Au cluster under the influence of atomic oxygen intermediates, leading to the formation of $Co_1O_2(OH)_2$ complex structures. This remarkable finding can be applied across a range of $Au_{54}M_1$ cluster systems, including metals like Co, Ni, Fe, Ru, Rh, Pd, Pt, Au, Cu, Zn, and Ir. We have developed a volcano plot for the ORR that showcases the activity of the $M_1O_x(OH)_y$ complex, with these results being substantiated by experimental data. This indicates that the $M_1O_x(OH)_y$ complex, formed during operational conditions, is the actual active site for the ORR. Our analysis suggests that the $Au_{54}Co_1$, $Au_{54}Cu_1$, and $Au_{54}Ru_1$ clusters are among the most effective Au-based SAA cluster catalysts for this reaction. The presence of stable $M_1O_x(OH)_y$ complexes in these SAA catalysts under ORR conditions demonstrates that intricate surface chemistry plays a significant role, thus redefining our understanding of the catalytic behavior of conventional metallic SAA models.

II. DFT CALCULATIONS

Spin-polarized density functional theory (DFT) calculations were conducted by using the Vienna *ab initio* simulation package (VASP) code [48, 49]. We used projector augmented wave (PAW) potentials [50] and utilized the Perdew–Burke–Ernzerhof (PBE) functionals [51]. During the cluster calculations, we placed the 55-atom Au clusters in a vacuum box with cell dimensions of 16.34 Å × 16.34 Å × 16.34 Å. The octahedral Ag_{55} clusters generally exhibit (111)-like surfaces. The Brillouin zone was sampled with a 1×1×1 Monkhorst–Pack k-point. The energy cut-off for the plane wave basis set was set at 350 eV during structure optimization, and the geometry optimization was considered complete when the forces on each atom were less than 0.05 eV/Å with a convergence threshold of 10^{-4} eV.

We first calculated the number of O atoms that could adsorb on the single-atom alloy using the following equation:

$$G_{\mathrm{ads\_O}} = G_{\mathrm{Au_{54}CoO_n}} - \frac{n}{2}G_{\mathrm{O_2}} - G_{\mathrm{Au_{54}Co}} \quad (1)$$

where $G_{\mathrm{Ag_{54}CoO_n}}$ and $G_{\mathrm{Ag_{54}Co}}$ are the calculated Gibbs free energies of $Ag_{54}CoO_n$ and $Ag_{54}Co$, respectively. $G_{\mathrm{O_2}}$ is the Gibbs free energy of the gaseous O_2 molecule. The Gibbs free energy of gaseous O_2 molecule is calculated using the formula $G(\mathrm{O_2(g)}) = 2\times(G(\mathrm{H_2O(l)}) - G(\mathrm{H_2(g)})) + 4.92$ eV. Here, $G(\mathrm{H_2O(l)})$ and $G(\mathrm{H_2(g)})$ are the Gibbs free energies of a water molecule in the liquid phase and a hydrogen molecule in the gas phase, respectively. Additionally, the absorbed O* atom can react with water to produce absorbed hydroxyl groups ($\mathrm{Au_{54}CoO_x} + y\mathrm{H_2O} \rightarrow \mathrm{Au_{54}CoO_{x-y}(OH)_y} + y\mathrm{OH^-}$), calculated as follows:

$$G = G_{\mathrm{Au_{54}CoO_{x-y}(OH)_y}} + yG_{\mathrm{OH}} - yG_{\mathrm{H_2O}} - G_{\mathrm{Au_{54}CoO_x}} \quad (2)$$

where $G_{\mathrm{Au_{54}CoO_{x-y}(OH)_y}}$ and $G_{\mathrm{Au_{54}CoO_x}}$ are the calculated Gibbs free energies of the $Au_{54}CoO_{x-y}(OH)_y$ and $Au_{54}CoO_x$ species, respectively. $G_{\mathrm{H_2O}}$ and G_{OH} are the Gibbs free energies of H_2O and OH^- in solution, respectively.

Ab initio molecular dynamics (AIMD) simulations [52] were performed to reveal the dynamic structural evolution of a dump atom in the Ag cluster with different adsorbates (H_2O, O_2, OH, O). These simulations were carried out in the canonical ensemble (NVT) at 900 K with a time step of 0.5 fs.

DOI: 10.1063/1674-0068/cjcp2405078 © 2024 Chinese Physical Society

III. RESULTS AND DISCUSSION

Before we reveal the ORR activity of Au alloy cluster, we have to determine its real structure and active site under reaction condition. We initially performed the thermodynamic analysis on the "magic-numbered" $Au_{54}Co_1$ cluster, comprising 55 atoms with density functional theory (DFT) calculations. This specific cluster size was selected due to its diameter, approximately 1.1 nm, which is akin to those frequently synthesized in experimental settings [53–57]. Theoretical models have established that for gold nanoparticles smaller than 1 nm, an icosahedral structure with exposed Au(111) facets is the most stable configuration [58, 59]. Accordingly, we utilize this configuration for our 55-atom Au cluster. We found the free energy of the structure where Co located at the cluster is 0.98 eV higher than that with Co inside the cluster. Our findings indicated that, in comparison to being positioned on the cluster surface, a single cobalt atom shows a preference for localization within the core of the $Au_{54}Co_1$ cluster. Consequently, there is a dearth of Co atoms on the surface of the $Au_{54}Co_1$ cluster in a vacuum. Given that the principal kinetic energy barrier for the ORR on Au catalysts involves the initial endothermic reduction of O_2, resulting in the formation of an adsorbed OOH* intermediate and the final OH* desorption energy, our investigation concentrated on examining the interactions of O_2*, O*, and OH* on the $Au_{54}Co_1$ cluster. Our results demonstrated that the intermediate O* could adsorb slightly exothermically on the surface of the $Au_{54}Co_1$ cluster, with an energy level of −0.53 eV with referred to O_2 molecule in the gas phase, indicating that oxygen atoms can position themselves near the cluster surface. Conversely, the other intermediates, O_2* and OH*, tend to remain distant from the Au cluster due to their weak adsorption strengths, with energy levels of −0.05 eV and 1.53 eV, respectively (FIG. 1).

The adsorption energies of the intermediates O_2*, O*, and OH* on the $Au_{54}Co_1$ cluster, with the cobalt atom positioned on the surface, were also evaluated. These oxygen-containing species may trigger the restructuring of $Au_{54}Co$ due to the strongly negative adsorption energies of O_2* and O* at the cobalt site (−1.21 eV and −1.51 eV, respectively), suggesting a strong affinity for oxygen species to bind to the surface at the Co site. As a result, the robust attachment of O_2* and O* to the cobalt atom can thermodynamically drive the migration of cobalt atoms from the interior to the surface of the $Au_{54}Co_1$ cluster. However, the binding energy of OH* at the cobalt site (E_{OH} = −0.06 eV) is insufficient to offset the energy required for the Co atom to migrate from the core to the surface of the $Au_{54}Co_1$ cluster.

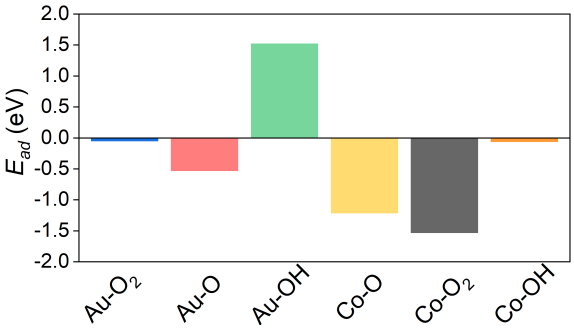

FIG. 1 Calculated adsorption energies of O*/O_2* and OH* species at the surface Au site and Co site of the $Au_{54}Co_1$ cluster with respect to gaseous O_2 and OH* in solution, respectively. The cohesive energy between Co and Au in the $Au_{54}Co_1$ cluster was also calculated based on the equation Au_{55}+Co_1(bulk)→$Au_{54}Co_1$+Au_1(bulk). All energies are in eV.

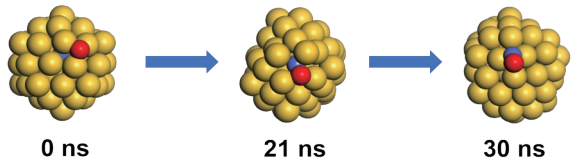

FIG. 2 Snapshot of the neural network potential MD simulation depicting O* adsorption on the $Au_{54}Co_1$ cluster to investigate the dynamic reconstruction of alloy cluster for 30 ns at 400 K. The yellow, blue, and red spheres are Au, Co, O atoms, respectively.

At an elevated temperature of 400 K, machine learning-accelerated molecular dynamics (MD) simulation were performed to elucidate the propensity for Co migration from the core to the surface of the $Au_{54}Co_1$ cluster, driven by the robust binding interactions of O_2* and O* with the Co atom. The choice of 400 K was strategically made to expedite the MD simulation process. We found there is a rapid migration of the Co atom from the core of the cluster to its surface within 30 ns, as illustrated in FIG. 2. This phenomenon can be ascribed to the low coordination number of gold atoms within the SAA $Au_{54}Co_1$ cluster, which enhances atomic mobility, thereby enabling subsurface cobalt atoms to migrate to the surface for O* adsorption. This migration facilitates the formation of more thermodynamically stable $Au_{54}Co_1O_x$ complexes.

Our calculation shows endothermic Gibbs free energy for the adsorption of OOH* intermediates on

DOI: 10.1063/1674-0068/cjcp2405078 © 2024 Chinese Physical Society

Au(111), making it less active to the ORR (Table S3 in Supplementary materials, SM). Given the pronounced binding affinity between the Co atom and oxygen-containing species, there is a heightened probability for additional O* and/or OH* molecules to adsorb at the Co site upon its migration from the cluster's core to its surface. To further elucidate this phenomenon, we conducted an advanced *ab initio* thermodynamic analysis to quantify the number of O* atoms (x) or OH* species (y) contributing to the formation of $Au_{54}Co_1O_x(OH)_y$ clusters under operational ORR conditions, employing the following equation:

$$Au_{54}Co_1 + \left(\frac{x}{2} + \frac{y}{2}\right) O_2 + yH_2O + ye^- \rightarrow Au_{54}Co_1O_x(OH)_y + yOH^- \quad (3)$$

The number of O containing species that Co site can hold is finite, because the binding strength of each oxygen species is gradually weakened, as the number of oxygen atoms increased, depicted in FIG. 3. This led to the attachment of O* and/or OH* molecules to the Co atom site during the formation of $Co_1O_x(OH)_y$ complexes. If the ΔG value of O species adsorption is above zero, we believe no more oxygen could adsorb on the Co site. Notably, we observed that at most four oxygen atoms can absorb on the Co atom (Co_1O_4) before the change in Gibbs free energy for further oxygen species adsorption became positive. Though the Gibbs free energy of the addition of the fourth oxygen is negative, the space around Co site is already saturated. Steric effect would prevent the adsorption of the fifth oxygen. *O is not the only adsorbate on Co site, it worths noting that the adsorbed O* molecules reacted with water, resulting in the exothermic generation of adsorbed OH* species. Our findings indicate adsorbed O* atom could transform into adsorbed OH* and finally form the most stable $Co_1O_2(OH)_2$ configuration under operational ORR conditions (as illustrated in FIG. 3 and Table S2 (SM)). $Au_{54}Co_1O_x(OH)_y$ cluster exhibits a nearly neutral Gibbs formation energy over bulk Au and Co by 0.06 eV due to the strong interactions between Co and O/OH intermediates, which demonstrate the high stability of $Au_{54}Co_1O_x(OH)_y$ cluster under operando condition.

In this study, we focused on the ORR activity over the $Au_{54}Co_1O_2(OH)_2$ cluster, finding that the inclusion of implicit water introduces negligible changes of less than 0.13 eV to the ORR energy landscape. This minimal impact justifies our approach to using the $Au_{54}Co_1O_2(OH)_2$ cluster to explore intrinsic catalytic behaviors. The solvent effect is neglected in the present work. To understand the ORR mechanism and the associated scaling relationships, it is essential to delve into the interplay between the adsorption energies of reaction intermediates and the catalytic activity of the surface. The ORR generally proceeds via a series of proton-coupled electron transfer steps, typically involving intermediates such as OOH*, O*, and OH*. The performance of an ORR catalyst is significantly influenced by its ability to balance the adsorption energies of these intermediates [11, 60]. A comprehensive investigation of the ORR mechanism was undertaken for the most stable $Co_1O_2(OH)_2$ complexes in an alkaline solution, as illustrated in FIG. 4 and FIG. 5. We meticulously calculated the ORR potential energy surfaces on Pt(111), Au(111), and CoO(111) surfaces as references were chosen due to their prevalent application in ORR research. At an electrode potential of 0.80 V versus the reversible hydrogen electrode (RHE), the Gibbs free energy change for the formation of the OOH* intermediate (ΔG_{OOH}) on Pt(111) is 0.23 eV, signifying an endothermic reaction. Concurrently, the Gibbs free energy change for the desorption of OH* (ΔG_{OH}) is –0.26 eV, indicating a spontaneous process. These values suggest that Pt(111) maintains an optimal balance, as neither the formation nor the desorption processes are overly favoured, which is crucial for high ORR activity (see FIG. 5 and Table S3 (SM)). On the Au(111) surface, the

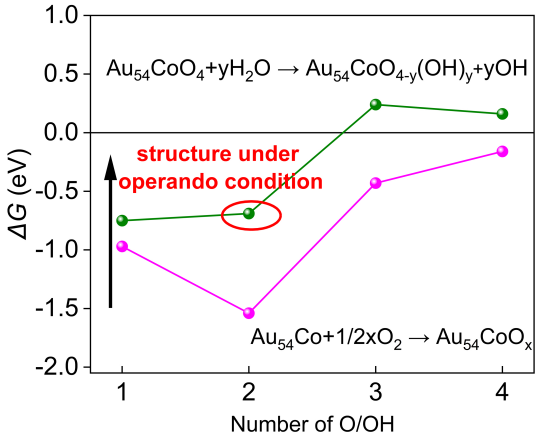

FIG. 3 Phase diagram of $Co_1O_x(OH)_y$ complexes obtained by *ab initio* thermal dynamic analysis. The purple line represents the Gibbs energy of different numbers of oxygen residing on the $Au_{54}Co$ cluster surface to form $Au_{54}CoO_x$ complex. The green line represents the Gibbs energy of different numbers of H_2O to react with $Au_{54}CoO_x$ complex to form $Au_{54}CoO_{4-y}(OH)_y$.

DOI: 10.1063/1674-0068/cjcp2405078 © 2024 Chinese Physical Society

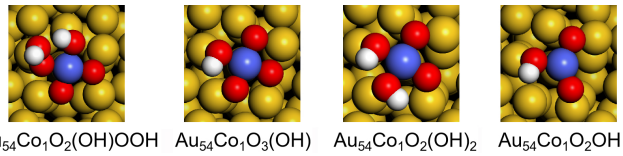

FIG. 4 Configurations of ORR intermediates of $Au_{54}Co_1O_x(OH)_y$ complexes. The yellow, blue, red and white spheres are Au, Co, O and H atoms, respectively.

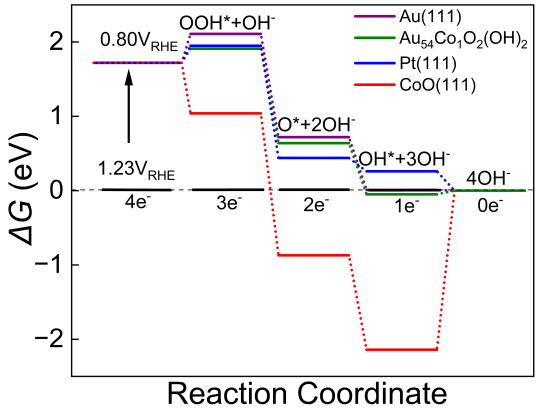

FIG. 5 Potential energy diagram for the ORR over the $Au_{54}Co_1O_2(OH)_2$, Au(111), Pt(111) and CoO(111) surfaces, the color is green, purple, blue, red, respectively.

reduced ORR activity compared to the Pt(111) surface is primarily due to the higher formation energy of the OOH* intermediates. The formation energy of OOH* on Au(111) is 1.04 eV more positive than on Pt(111) (see Table S3 (SM)). This significant increase in energy indicates that OOH* intermediates are less stable on Au(111), making it less favorable for the initial steps of the ORR. Consequently, the weaker binding of OOH* intermediates results in a lower overall catalytic activity for the ORR on the Au(111). In contrast, the CoO(111) surface displays markedly inferior ORR activity compared to Pt(111), which can be attributed to the excessively strong adsorption of OH* intermediates, with a ΔG_{OH} value of −2.14 eV. This strong adsorption indicates that OH* intermediates bind too tightly to the CoO(111) surface, effectively blocking the reactive sites and preventing the further progression of the ORR. Unlike Au(111) and CoO(111), the $Co_1O_2(OH)_2$ complex exhibits moderate binding energies for these intermediates. The $Co_1O_2(OH)_2$ complex's ability to strike this balance sets it apart, making it a more effective catalyst for the ORR compared to both the Au(111) and CoO(111) surfaces (FIG. 5 and Table S3 (SM)).

The limiting potential U_L of ORR reaction is calculated based on the free energy of each step of ORR. The U_L value signifies the requisite external voltage for each reaction step to proceed spontaneously, serving as a pivotal criterion for evaluating catalyst reactivity. The U_L of the $Co_1O_2(OH)_2$ complex was determined to be 0.58 eV, which exceeds that of Au(111) (measured at −0.24 eV) and CoO(111) (measured at −1.34 eV), as well as Pt(111) (measured at 0.57 eV). Consequently, the $Co_1O_2(OH)_2$ complex demonstrated superior ORR activity in comparison to the Pt(111), Au(111), and CoO(111) surfaces. Therefore, the $Au_{54}Co_1$ cluster emerges as a promising catalyst for facilitating the ORR under alkaline conditions, primarily attributed to the presence and exceptional reactivity of the $Co_1O_2(OH)_2$ complex.

Since we have observed the dynamic formation of complex like active site on $Au_{54}Co_1$ cluster, we have to check the active site of other Au-based alloy cluster before we predict their ORR activity. To determine whether the generation of $Co_1O_2(OH)_2$ under ORR conditions is an isolated phenomenon or a universal principle applicable to other metals, we extended our investigation to the stability of nine additional $Au_{54}M_1$ clusters, where M represents various metals including Fe, Ni, Ru, Rh, Pd, Pt, Au, Cu, Zn, and Ir, under ORR conditions. First-principles thermodynamic analysis indicates that the strong adsorption of O* species at the M_1 site (with E_O values ranging from −0.13 eV to −2.82 eV, see Table S4 (SM)) could drive the migration of the M_1 site from the core to the surface thermodynamically. In this study, we did not consider the dynamics of clusters and their impact on the ORR, which occurs at the $M_1O_x(OH)_y$ complexes within the icosahedral structure. The determination of the number of O* and OH* groups in the operationally generated $M_1O_x(OH)_y$ complexes was carried out using the same methodology employed for $Co_1O_2(OH)_2$, as previously discussed (refer to Tables S4,S5 and FIGs. S2,S3 in SM). This comprehensive analysis underscores the potential universality of the observed phenomenon, where the presence of strongly adsorbed O* species at the metal sites within these clusters facilitates the formation of stable $M_1O_x(OH)_y$ complexes, thereby enhancing ORR activity across a diverse range of metals.

The volcano plot, a well-recognized concept in the domain of ORR activity and oxygen adsorption strength (E_{OH^*}), highlights the importance of an ideal catalyst—where the adsorption strength of key intermediates strikes a precise balance, neither too weak nor too

DOI: 10.1063/1674-0068/cjcp2405078 © 2024 Chinese Physical Society

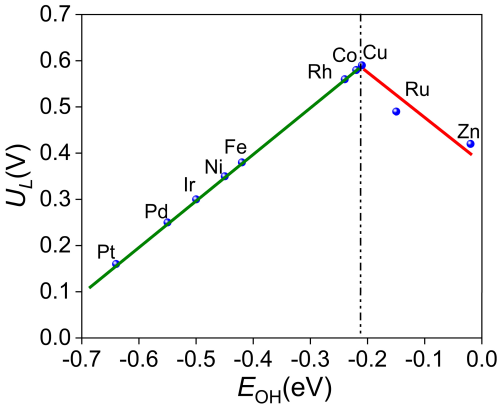

FIG. 6 Volcano plot of the U_L of the $Au_{54}M_1O_x(OH)_y$ complexes formed under operational ORR conditions (M=Co, Ni, Fe, Cu, Ru, Rh, Zn, Pt, Pd, and Ir).

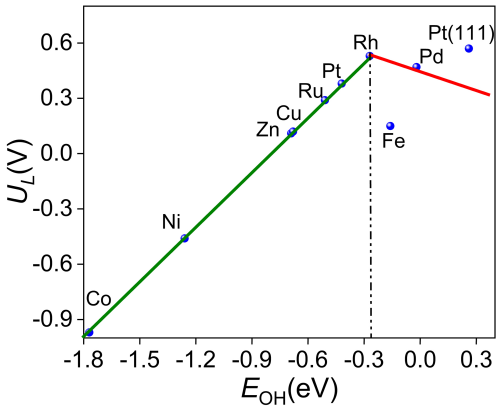

FIG. 7 Volcano plot of the U_L of the metallic Pt(111) surface and $Au_{54}M_1$ cluster, where a single M atom is located on the surface of the cluster (M=Co, Ni, Fe, Cu, Ru, Rh, Zn, Pt, and Pd).

strong. Intriguingly, similar to what has been observed on a pristine metal surface, we observed a similar volcano plot for both the $Au_{54}M_1O_x(OH)_y$ complexes (FIG. 6) and metallic $Au_{54}M_1$ clusters (FIG. 7), where the ORR activity altered according to the OH* adsorption energy (E_{OH*}) [60]. Metals characterized by weak interactions with OH* are situated on the left flank of the volcano plot, whereas those with robust interactions occupy the right flank. The summit of the volcano plot signifies the highest ORR activity, indicating that an ideal ORR catalyst should exhibit moderate binding energy with OH*. This equilibrium in OH* binding strength, located at the apex of the E_{OH*} volcano plot, epitomizes a highly effective ORR catalyst. Such a balance ensures that the catalyst does not bind OH* too weakly, which would hinder the reaction, nor too strongly, which would saturate active sites and impede further reaction progression. Achieving this optimal binding energy is paramount for maximizing catalytic efficiency and enhancing performance in the ORR.

It is noteworthy that the ORR activity exhibits significant variability across different $Au_{54}M_1$ clusters, underscoring the critical role of single-atom doping in modulating catalytic activity for the ORR. Among these complexes, the $Co_1O_2(OH)_2$ complex demonstrates the highest ORR activity, with an U_L value reaching 0.58 V. The superior activity of the $Co_1O_2(OH)_2$ complex, surpassing that of the Pt(111) surface, suggests that $Au_{54}Co_1$ clusters could potentially supplant platinum catalysts for ORR reactions in alkaline environments. Additionally, the $Au_{54}Rh_1(OH)_3$ and $Au_{54}Cu_1(OH)_2$ complexes exhibit U_L values (0.56 V and 0.59 V, respectively) comparable to that of platinum, indicating their high ORR activity. Conversely, the $Au_{54}Pt_1(OH)_4$ and $Au_{54}Pd_1(OH)_4$ clusters show lower ORR activity, with U_L values approximating 0.20 V, primarily due to the stronger adsorption of OH* intermediates on these clusters, which hinders the reaction. Furthermore, the $Au_{54}Zn_1(OH)_2$ cluster also displays low ORR activity, with a U_L value of 0.42 V, attributed to its weak adsorption of OH*, resulting in a higher energy barrier for the formation of the basic OOH* intermediate. In summary, $Au_{54}Co_1$, $Au_{54}Rh_1$, and $Au_{54}Cu_1$ clusters are theoretically predicted to be highly active ORR alloy catalysts, owing to their optimal binding energies and superior performance metrics, making them promising candidates for future catalytic applications in alkaline environments.

Previous investigations have predominantly employed pure metallic alloy clusters to simulate catalysts under real-world reaction conditions. However, significant discrepancies in catalytic behavior emerge when comparing the volcano plots of the $Au_{54}M_1O_x(OH)_y$ and $Ag_{54}M_1$ models. These conventional metallic alloy models often fall short in accurately predicting the ORR activity observed experimentally. For instance, the metallic $Au_{54}Co_1$ cluster exhibits a strongly negative OH* adsorption energy ($E_{OH*}=-1.26$ eV) (see Table S7 (SM)), leading to markedly reduced ORR activity with a U_L of −0.46 V (see Table S8 (SM)). In stark contrast, when configured as an $Au_{54}Co_1O_2(OH)_2$ cluster, $Co_1O_2(OH)_2$ demonstrates significantly enhanced ORR activity, with an OH* desorption energy close to 0 eV ($U_L=0.58$ V). This pronounced disparity underscores the necessity of determining the true catalytic configuration under operational conditions by juxtaposing calculated ORR activities with empirical results.

DOI: 10.1063/1674-0068/cjcp2405078 © 2024 Chinese Physical Society

We predict $Au_{54}Co_1O_2(OH)_2$, $Au_{54}Rh_1(OH)_3$ and $Au_{54}Cu_1(OH)_2$ SAA clusters as promising ORR catalysts. Numerous experimental investigations have identified AuCo alloy clusters as exemplary ORR catalysts [39]. Recent studies have highlighted the efficacy of carbon-supported bimetallic AuCo alloy electrocatalysts, which exhibit a specific activity 5% higher than that of Au/C at 0.85 V *vs.* RHE [61]. This improvement in activity underscores the potential of bimetallic systems in electrocatalytic applications. Moreover, AuCu alloys have also garnered attention as viable candidates for the ORR [62, 63], demonstrating their superior catalytic performance. Additionally, oxidized AuRh nanoparticles have shown remarkable ORR activity, outperforming pure Rh by a factor of five [64]. The consistent agreement between experimental results and theoretical predictions confirms that the $Rh_1O_x(OH)_y$ complexes are likely the active sites in these Au-based alloy clusters during ORR, highlighting their crucial role in enhancing the catalytic efficiency. Notably, experimental observations are consistent with the behavior predicted by the $Au_{54}M_1O_x(OH)_y$ model under reaction conditions, which cannot be adequately elucidated by the conventional metallic $Au_{54}M_1$ model alone. This insight accentuates the critical importance of the $Au_{54}M_1O_x(OH)_y$ complex in forecasting the catalytic performance of alloy clusters for the ORR. Our findings contribute to a deeper understanding of the significance of these complexes formed under operational ORR conditions, indictating the catalytic behavior of alloy catalysts during the ORR process.

To expound the significant contrast in ORR activity between the $Au_{54}Co_1O_2(OH)_2$ complex and the $Au_{54}Co_1$ cluster, we conducted an in-depth electronic analysis to unravel the superior activity of the $Au_{54}Co_1O_2(OH)_2$ complex relative to the metallic $Au_{54}Co_1$ cluster. Crystal orbital Hamilton population (COHP) analysis indicates a greater number of bonding orbitals between Co and O* in OH* are occupied on the $Au_{54}Co_1$ surface compared to the $Au_{54}Co_1O_2(OH)_2$ complex. This results in a reduced integrated COHP (ICOHP) for the Co–O bond in the $Au_{54}Co_1O_2(OH)_2$ complex, as shown in FIG. S4 (SM). Consequently, OH* displays a moderate affinity for adsorption on the $Au_{54}Co_1O_2(OH)_2$ complex, contrasting with the higher binding strength observed on the metallic $Au_{54}Co_1$ cluster. The increased binding on the metallic $Au_{54}Co_1$ leads to a reduced ORR activity due to the poisoning effect on the cluster, where the strong adsorption of OH* intermediates blocks active sites and hinders the reaction. Our research underscores the importance of considering the *in situ* formation of structures to accurately identify the active sites for the ORR. Understanding these dynamic transformations is crucial for optimizing catalyst design and enhancing catalytic performance, particularly in complex alloy systems where the active configurations may evolve under operational conditions.

IV. CONCLUSION

First-principles calculations confirm that the $Au_{54}M_1O_x(OH)_y$ complex is the key active site for driving the ORR in gold-based single-atom alloy cluster catalysts. This finding is substantiated by a volcano plot corresponding to the $M_1O_x(OH)_y$ complex, which concurs with experimental data and highlights the shortcomings of traditional models that fail to accurately identify the metallic Au-based SAA clusters. Particularly, the plot indicates the high activity of $Au_{54}Co_1$, $Au_{54}Rh_1$, and $Au_{54}Cu_1$ as alloy cluster catalysts. This research emphasizes the importance of applying theoretical modeling, taking into account the specific reaction conditions, to accurately identify the true active sites. These insights enhance our comprehension of the structures and mechanisms of the $Au_{54}M_1O_x(OH)_y$ clusters in ORR environments, providing crucial information for the design of more effective catalysts across various catalytic applications.

Supplementary materials: Detailed calculation methodology, calculated energetics, calculated configurations, and electronic structure analysis are shown.

V. AUTHOR CONTRIBUTIONS

Jin-Xun Liu conceived the idea and supervised and directed the project. Yixuan Pu performed the theoretical calculations and analysed the DFT data. All the authors discussed the results, and wrote and commented on the paper.

VI. NOTES

The authors declare no conflicts of interest.

VII. ACKNOWLEDGEMENTS

This work was supported by the Key Technologies

 © 2024 Chinese Physical Society

R&D Program of China (2021YFA1502804), the Strategic Priority Research Program of the Chinese Academy of Science (XDB0450102), the National Natural Science Foundation of China (No.22172150, No.22221003 and No.22222306), the National Natural Science Foundation of Anhui Province (2108085QB62), the USTC Research Funds of the Double First-Class Initiative (YD2060002012), the Innovation Program for Quantum Science and Technology (2021ZD0303302) and high-performance computational resources provided by the University of Science and Technology of China and the Hefei Advanced Computing Center.

[1] A. Ali, S. Khandelwal, S. Panja, P. Majumder, and A. Dutta, *Oxygen Reduction Reaction*, K. Sengupta, S. Chatterjee, and K. Dutta Eds., Amsterdam: Elsevier, 1 (2022). DOI: 10.1016/B978-0-323-88508-9.00013-6.
[2] M. Y. Liu, X. D. Xiao, Q. Li, L. Y. Luo, M. H. Ding, B. Zhang, Y. X. Li, J. L. Zou, and B. J. Jiang, J. Colloid Interface Sci. **607**, 791 (2022).
[3] X. Q. Wang, Z. J. Li, Y. T. Qu, T. W. Yuan, W. Y. Wang, Y. E. Wu, and Y. D. Li, Chem **5**, 1486 (2019).
[4] L. L. Chen, X. L. Xu, W. X. Yang, and J. B. Jia, Chin. Chem. Lett. **31**, 626 (2020).
[5] J. Y. Zhang, C. Xia, H. F. Wang, and C. Tang, J. Energy Chem. **67**, 432 (2022).
[6] R. G. Ma, G. X. Lin, Y. Zhou, Q. Liu, T. Zhang, G. C. Shan, M. H. Yang, and J. C. Wang, npj Comput. Mater. **5**, 78 (2019).
[7] Y. G. Zhao, D. P. Adiyeri Saseendran, C. Huang, C. A. Triana, W. R. Marks, H. Chen, H. Zhao, and G. R. Patzke, Chem. Rev. **123**, 6257 (2023).
[8] W. H. Zhao, G. T. Xu, W. Y. Dong, Y. W. Zhang, Z. P. Zhao, L. M. Qiu, and J. C. Dong, Adv. Sci. **10**, 2300550 (2023).
[9] C. Santoro, P. Bollella, B. Erable, P. Atanassov, and D. Pant, Nat. Catal. **5**, 473 (2022).
[10] J. Stacy, Y. N. Regmi, B. Leonard, and M. Fan, Renew. Sustain. Energy Rev. **69**, 401 (2017).
[11] X. M. Ge, A. Sumboja, D. Wuu, T. An, B. Li, F. W. T. Goh, T. S. A. Hor, Y. Zong, and Z. L. Liu, ACS Catal. **5**, 4643 (2015).
[12] W. Mabhulusa, K. E. Sekhosana, and X. Fuku, Int. J. Electrochem. Sci. **19**, 100524 (2024).
[13] M. H. Shao, Q. W. Chang, J. P. Dodelet, and R. Chenitz, Chem. Rev. **116**, 3594 (2016).
[14] M. Janssen, P. Weber, and M. Oezaslan, Curr. Opin. Electrochem. **40**, 101337 (2023).
[15] M. Inaba, A. Zana, J. Quinson, F. Bizzotto, C. Dosche, A. Dworzak, M. Oezaslan, S. B. Simonsen, L. T. Kuhn, and M. Arenz, ACS Catal. **11**, 7144 (2021).
[16] J. J. Zhao, C. H. Fu, K. Ye, Z. Liang, F. L. Jiang, S. Y. Shen, X. R. Zhao, L. Ma, Z. Shadike, X. M. Wang, J. L. Zhang, and K. Jiang, Nat. Commun. **13**, 685 (2022).
[17] J. Liu, M. G. Jiao, L. L. Lu, H. M. Barkholtz, Y. P. Li, Y. Wang, L. H. Jiang, Z. J. Wu, D. J. Liu, L. Zhuang, C. Ma, J. Zeng, B. S. Zhang, D. S. Su, P. Song, W. Xing, W. L. Xu, Y. Wang, Z. Jiang, and G. Q. Sun, Nat. Commun. **8**, 15938 (2017).
[18] K. Kodama, T. Nagai, A. Kuwaki, R. Jinnouchi, and Y. Morimoto, Nat. Nanotechnol. **16**, 140 (2021).
[19] P. Chandran, A. Ghosh, and S. Ramaprabhu, Sci. Rep. **8**, 3591 (2018).
[20] Y. Nie, L. Li, and Z. D. Wei, Chem. Soc. Rev. **44**, 2168 (2015).
[21] S. T. Li, X. S. Du, Z. Y. Liu, Y. W. Li, Y. C. Shao, and R. C. Jin, Precis. Chem. **1**, 14 (2023).
[22] M. K. Qin, M. H. Qi, R. X. Fan, J. D. Chen, X. Y. Shi, B. B. Lin, L. L. Xi, and Y. Wang, Precis. Chem. **1**, 497 (2023).
[23] Y. X. Pu, J. L. Chen, J. W. Zhao, L. Feng, J. Z. Zhu, X. C. Jiang, W. X. Li, and J. X. Liu, JACS Au (2024). DOI: 10.1021/jacsau.4c00116.
[24] Y. Nakaya and S. Furukawa, Chem. Rev. **123**, 5859 (2023).
[25] L. C. Liu and A. Corma, Chem. Rev. **118**, 4981 (2018).
[26] V. Ponec, Appl. Catal. A Gen. **222**, 31 (2001).
[27] C. Lim, A. R. Fairhurst, B. J. Ransom, D. Haering, and V. R. Stamenkovic, ACS Catal. **13**, 14874 (2023).
[28] S. F. Ji, C. Jun, Y. J. Chen, and D. S. Wang, Precis. Chem. **1**, 199 (2023).
[29] Z. Fang, W. T. Zhao, T. Shen, D. P. Qiu, Y. C. Lv, X. M. Hou, and Y. L. Hou, Precis. Chem. **1**, 395 (2023).
[30] B. Q. Ge, F. F. Wei, Q. Wan, H. W. Zhang, P. Yuan, and S. Lin, Precis. Chem. **1**, 429 (2023).
[31] J. Q. Su, J. Feng, Y. G. Feng, S. H. Liu, B. Y. Xu, Y. Lin, J. Y. Ye, Y. Zhang, Y. Y. Li, Q. Shao, and X. Q. Huang, Precis. Chem. **1**, 363 (2023).
[32] D. X. Yan, Y. X. Gao, M. Y. Qi, H. P. Jia, and Y. J. Xu, Precis. Chem. **1**, 299 (2023).
[33] L. B. Sun, V. Reddu, and X. Wang, Chem. Soc. Rev. **51**, 8923 (2022).
[34] X. Z. Li, S. Mitchell, Y. Y. Fang, J. Li, J. Perez-Ramirez, and J. Lu, Nat. Rev. Chem. **7**, 754 (2023).
[35] M. Peng, C. Y. Dong, R. Gao, D. Q. Xiao, H. Y. Liu, and D. Ma, ACS Cent. Sci. **7**, 262 (2021).
[36] J. Liu, D. Cao, H. X. Xu, and D. J. Cheng, Nano Select **2**, 251 (2021).
[37] E. C. Tyo and S. Vajda, Nat. Nanotechnol. **10**, 577 (2015).
[38] Y. X. Wang, M. D. Wei, Q. D. Ding, H. M. Li, and W. Ma, Nano Lett. **24**, 4733 (2024).
[39] L. M. Guo, D. F. Zhang, and L. Guo, Adv. Funct. Mater. **30**, 2001575 (2020).
[40] X. J. Zou, S. P. He, X. Kang, S. Chen, H. Z. Yu, S. Jin, D. Astruc, and M. Z. Zhu, Chem. Sci. **12**, 3660 (2021).

 © 2024 Chinese Physical Society

[41] R. T. Hannagan, G. Giannakakis, M. Flytzani-Stephanopoulos, and E. C. H. Sykes, Chem. Rev. **120**, 12044 (2020).
[42] M. T. Greiner, T. E. Jones, S. Beeg, L. Zwiener, M. Scherzer, F. Girgsdies, S. Piccinin, M. Armbrüster, A. Knop-Gericke, and R. Schlögl, Nat. Chem. **10**, 1008 (2018).
[43] W. Liu, H. S. Feng, Y. S. Yang, Y. M. Niu, L. Wang, P. Yin, S. Hong, B. S. Zhang, X. Zhang, and M. Wei, Nat. Commun. **13**, 3188 (2022).
[44] T. J. Zhang, A. G. Walsh, J. H. Yu, and P. Zhang, Chem. Soc. Rev. **50**, 569 (2021).
[45] Z. K. Han, D. Sarker, R. H. Ouyang, A. Mazheika, Y. Gao, and S. V. Levchenko, Nat. Commun. **12**, 1833 (2021).
[46] J. J. Mao, J. S. Yin, J. J. Pei, D. S. Wang, and Y. D. Li, Nano Today **34**, 100917 (2020).
[47] J. Li, H. M. Yin, X. B. Li, E. Okunishi, Y. L. Shen, J. He, Z. K. Tang, W. X. Wang, E. Yücelen, C. Li, Y. Gong, L. Gu, S. Miao, L. M. Liu, J. Luo, and Y. Ding, Nat. Energy **2**, 17111 (2017).
[48] G. Kresse and J. Hafner, Phys. Rev. B **47**, 558 (1993).
[49] G. Kresse and J. Furthmüller, Phys. Rev. B **54**, 11169 (1996).
[50] P. E. Blochl, Phys. Rev. B **50**, 17953 (1994).
[51] J. P. Perdew, K. Burke, and M. Ernzerhof, Phys. Rev. Lett. **77**, 3865 (1996).
[52] G. Pastore, E. Smargiassi, and F. Buda, Phys. Rev. A **44**, 6334 (1991).
[53] B. Weng, K. Q. Lu, Z. C. Tang, H. M. Chen, and Y. J. Xu, Nat. Commun. **9**, 1543 (2018).
[54] K. Y. Zheng, M. I. Setyawati, D. T. Leong, and J. P. Xie, ACS Nano **11**, 6904 (2017).
[55] J. Kong, W. Zhang, Y. Z. Wu, and M. Zhou, Aggregate **3**, e207 (2022).
[56] Y. M. Liu, H. Tsunoyama, T. Akita, and T. Tsukuda, J. Phys. Chem. C **113**, 13457 (2009).
[57] J. Liu, N. Jian, I. Ornelas, A. J. Pattison, T. Lahtinen, K. Salorinne, H. Häkkinen, and R. E. Palmer, Ultramicroscopy **176**, 146 (2017).
[58] F. Baletto and R. Ferrando, Rev. Mod. Phys. **77**, 371 (2005).
[59] H. Haouas, L. El Atouani, K. Sbiaai, and A. Hasnaoui, Comput. Mater. Sci. **214**, 111695 (2022).
[60] A. Kulkarni, S. Siahrostami, A. Patel, and J. K. Nørskov, Chem. Rev. **118**, 2302 (2018).
[61] F. Acosta-Arreazola, N. A. Garcia-Gomez, M. Chatenet, V. Martin, I. López, and E. M. Sánchez, Mater. Chem. Phys. **278**, 125605 (2022).
[62] H. Q. Chen, M. Nishijima, G. J. Wang, S. Khene, M. Q. Zhu, X. Deng, X. M. Zhang, W. Wen, Y. Luo, and Q. G. He, J. Electrochem. Soc. **164**, F1654 (2017).
[63] N. L. Zhang, X. Chen, Y. J. Lu, L. An, X. Li, D. G. Xia, Z. Zhang, and J. X. Li, Small **10**, 2662 (2014).
[64] K. Akiyoshi, Y. Watanabe, T. Kameyama, T. Kawawaki, Y. Negishi, S. Kuwabata, and T. Torimoto, Phys. Chem. Chem. Phys. **24**, 24335 (2022).

DOI: 10.1063/1674-0068/cjcp2405078 © 2024 Chinese Physical Society